Model Based 3D Segmentation and OCT Image Undistortion of Percutaneous Implants

Oliver Müller[1], Sabine Donner[2,3], Tobias Klinder[4], Ralf Dragon[1], Ivonne Bartsch[3], Frank Witte[3], Alexander Krüger[2,3], Alexander Heisterkamp[2,3], and Bodo Rosenhahn[1,⋆]

[1] Institut für Informationsverarbeitung, Leibniz Universität Hannover, Appelstraße 9a, 30167 Hannover, Germany
{omueller,rosenhahn}@tnt.uni-hannover.de
[2] Laser Zentrum Hannover e.V., Hollerithallee 8, 30419 Hannover, Germany
[3] CrossBIT, Center for Biocompatibility and Implant-Immunology, Hannover Medical School, Feodor-Lynen-Straße 31, 30625 Hannover, Germany
[4] Philips Research North America, Briarcliff Manor, NY 10510, USA

Abstract. Optical Coherence Tomography (OCT) is a noninvasive imaging technique which is used here for in vivo biocompatibility studies of percutaneous implants. A prerequisite for a morphometric analysis of the OCT images is the correction of optical distortions caused by the index of refraction in the tissue. We propose a fully automatic approach for 3D segmentation of percutaneous implants using Markov random fields. Refraction correction is done by using the subcutaneous implant base as a prior for model based estimation of the refractive index using a generalized Hough transform. Experiments show the competitiveness of our algorithm towards manual segmentations done by experts.

1 Introduction

Optical Coherence Tomography is a non invasive imaging modality used for taking optical biopsies of layered tissue structures such as the epidermis [11] and the retina [4,14]. Apart from clinical use, OCT also has applications in animal studies with the advantage of repetitive biopsies at one animal at different time points instead of lethal biopsies at different animals for each time point. The particular objective of this study is the morphometric analysis of the skin in the vicinity of a percutaneous implant situated in the lateral abdominal region of a hairless mouse to draw conclusions on its biocompatibility (see Fig. 1(a)).

As the optical properties of the tissue introduce distortions into the OCT images [13], segmentation based image undistortion is an important step towards fully automatic image analysis tasks. In recent works, several methods like graph based global optimization, active contours and random fields are proposed for layer segmentation. In practice, graph based approaches, as used in [5] for fully

⋆ This work has been partially funded by the DFG within the excellence cluster REBIRTH.

G. Fichtinger, A. Martel, and T. Peters (Eds.): MICCAI 2011, Part III, LNCS 6893, pp. 454–462, 2011.

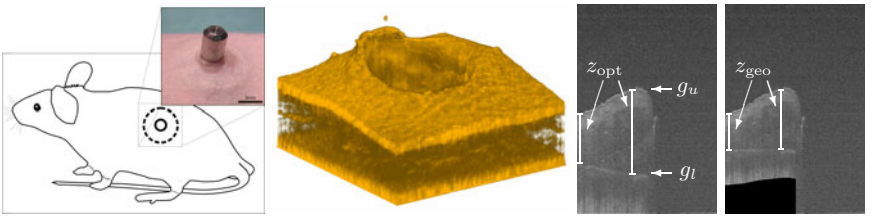

Fig. 1. (a) Location and photo of a percutaneous implant, (b) OCT dense 3D scan volume rendering (percutaneous pin is not visible), (c) single OCT B-scan (cropped at half) showing the distorted baseline, and (d) corresponding undistorted result

automatic 3D retinal multilayer segmentation, lead to huge graph sets, limiting the number of voxels. Active contour models (e.g. snakes) [9,14] provide robust results, however require manual initialization. In [8], a fully automatic 2D feature segmentation is presented using conditional random fields and efficient optimization algorithms for inference. Segmentation of a single 2D OCT scan (B-scan) can be susceptible to local shading effects and image perturbations and extending the scanning scheme to the third dimension can significantly improve the segmentation quality [3,5,6]. Thus our algorithm is based on 3D segmentation.

This paper proposes an approach for fully automatic segmentation of 3D Fourier-domain OCT and refractive undistortion. The determination of the refractive index is facilitated by the geometry of the implant which consists of a percutaneous pin (3 mm diameter and 5 mm length) anchored beneath the dermis by a flat disc shaped base which is visible in OCT (see Fig. 1(a)–(d)).

Two main technical **contributions** are proposed. First, estimation of the skin surface in the 3D space from several OCT B-scans is done using a Markov random field (MRF) approach with an efficient combination of global and local optimization algorithms. A spoke pattern scanning scheme is used for 3D data acquisition and is further compared with a dense 3D scanning scheme (see Fig. 2(a)). Our second contribution addresses the segmentation of the implant base. The distorted implant base is segmented using a refractive distortion model and the previously segmented skin surface for parameter estimation in order to match the distorted implant base best to the a priori known shape of the undistorted base contour. The parameters of the implant base are estimated with a fast generalized 3D Hough transform approach, optimizing the refractive index, as well as the 3D position and orientation of the implant base. The segmented model is finally used for refractive image undistortion (see Fig. 1(c)–(d)).

In Section 2, the 3D segmentation of the pin position, the skin surface and the implant base is described (Fig. 2(b)), which is used for refractive image undistortion (Fig. 2(c)). In Section 3, the used undistortion model is verified and a comparison of the spoke pattern and dense 3D scanning scheme is shown, followed by a quantitative analysis of several mouse datasets segmented and undistorted using our method. Finally, in Section 4, a short conclusion is given.

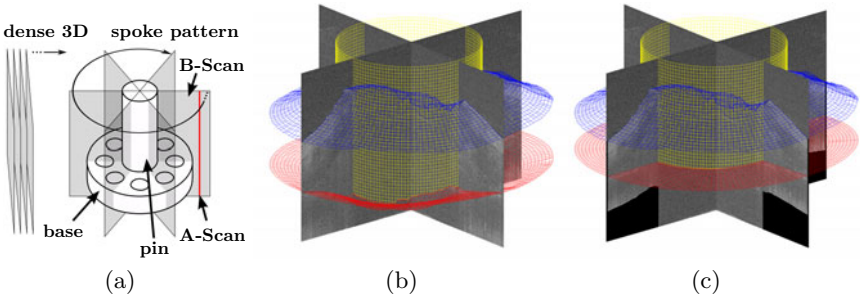

Fig. 2. (a) Schematic of the percutaneous implant (pin and base) and OCT scanning schemes (dense 3D and spoke pattern), (b) two orthogonal OCT B-scans with segmentation (mesh overlay) of pin position (yellow), skin surface (blue) and deformed base (red), (c) undistorted B-scans with mesh overlay

2 Methods

The OCT data is acquired in a sequence of B-scans $(I^k)_{k=1,\ldots,K}$ (see Fig. 2(a)) with image width W and height H. To reduce noise and small scanning artifacts, while preserving edges, we apply a median filter to each B-scan as a first preprocessing step. In a second step, we apply a pixel intensity normalization to each image, leading to a zero-mean intensity distribution with unit variance, in order to retrieve uniform edge responses from the later applied edge filter. We use a Sobel filter in combination with a presmoothing Gaussian kernel with $\sigma_{\text{gauss}} = 1.5$ to get first order derivative images I^k_{x} and I^k_{y} in x- and y-direction of I^k.

For 3D segmentation, the two-dimensional B-scans are embedded in a global 3D coordinate system. A mapping of a 3D point position $\boldsymbol{P} = (X, Y, Z)$ into image coordinates $\boldsymbol{p} = (x, y)$, i.e. $(X, Y, Z) \mapsto (k, x, y)$ as shown in Fig. 3(a) is done, resulting in a sparse volume representation $V(X, Y, Z) = I^k(x, y)$ for the image intensities. The volumes of the image derivatives V_{x}, and V_{y} are analogously defined, using I^k_{x} and I^k_{y} instead of I^k.

The proposed implant segmentation method is divided into three consecutive steps (see Fig. 2(b)–2(c)): The pin segmentation (yellow cylinder), the skin surface segmentation (blue mesh), and the base segmentation (red mesh).

2.1 Pin Segmentation

In the image area where the implant pin is located, there is no tissue, and hence no contour information. Therefore, this area can be ignored for following segmentation steps. The pin is of cylindrical form and the diameter d is known a priori. The diameter is allowed to have a variance v^k of ± 10 pel. For each image I^k, the x-position of the left and right pin boundary x^k_1 and $x^k_2 = x^k_1 + d + v^k$ is computed using a generalized Hough transform [1] approach over $I^k_{\text{acc}}(x) = \sum_y |I^k_{\text{x}}(x, y)|$

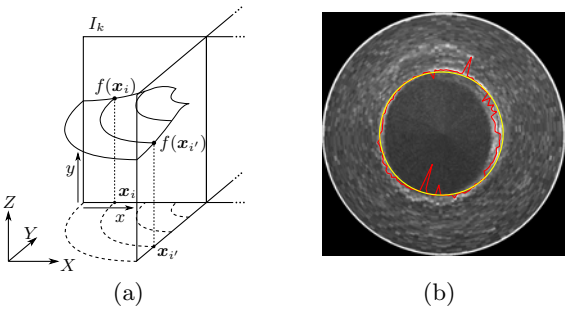

Fig. 3. (a) Modeling of skin surface f over grid points $\boldsymbol{x}_i, \boldsymbol{x}_{i'}$ with respect to global coordinate system (X, Y, Z) using spoke pattern scanning scheme, (b) top view of accumulated image intensities I_{acc} and segmented pin boundary for each B-scan individually (red), and with fitted cylinder (yellow)

with $\max_{x_1^k, v^k} \left[I_{\text{acc}}^k(x_1^k) + I_{\text{acc}}^k(x_1^k + d + v^k) \right]$. The pin estimation in a single B-scan is susceptible to noise and vanishing of boundary contours (see Fig. 3(b), red line). Therefore, the boundaries are smoothed by assuming a cylindrical form and radius r of the pin: At first, the center position $\boldsymbol{C} = (C_X, C_Y)$ of the pin in the XY-plane is calculated as the arithmetic mean of all boundary positions $\boldsymbol{B}_1^k$ and $\boldsymbol{B}_2^k$ corresponding to x_1^k and x_2^k, i.e. $\boldsymbol{C} = \frac{1}{2K} \sum_k (\boldsymbol{B}_1^k + \boldsymbol{B}_2^k)$. Then, the radius r is computed as the median of all radians $r = \text{median}(|\boldsymbol{C}\boldsymbol{B}_1^1|, \ldots, |\boldsymbol{C}\boldsymbol{B}_1^K|)$. The yellow line in Fig. 3(b) shows a typical result of the pin segmentation step.

2.2 Skin Modeling and Segmentation

A correct estimation of the skin surface is crucial for a correct modeling of the implant base. The skin surface, denoted as $f(X, Y) = Z$, is assumed to be smooth and to behave like a membrane, thus having no discontinuities, except the pinhole. Several approaches can be used to model the surface: Markov Random Fields (MRF), Conditional Random Fields or Discriminative Random Fields [10]. Due to the smoothness property, we decided to use an adapted MRF for segmentation of the skin surface. Following the notations in [10], the posterior probability of the skin surface f given the volumetric pixel intensities V can be written as $P(f \mid V) \propto P(f, V) = p(V \mid f)P(f)$ using the Maximum A-Posteriori framework (MAP), where $P(f)$ is the smoothness prior and $p(V \mid f)$ denotes the likelihood function of f for V fixed.

To represent probabilistic relationships of the MRF, a common graphical notation is used. The neighborhood relationships of a MRF can be described given a graph $G = (V, E)$ with a set of nodes V representing the instances of the random field and a set of edges E representing the conditional dependencies between the instances. The prior probability is then modeled as follows:

$$P(f) = \exp\left[-\textstyle\sum_{i \in V} U(f_i)\right] \quad \text{with} \quad U(f_i) = \textstyle\sum_{\{i,i'\} \in E} (f_i - f_{i'})^2 / 2\sigma_s^2 \ , \quad (1)$$

where σ_s is a constant weighting factor. Figure 3(a) shows the relation of the skin surface $f_i = f(\boldsymbol{x}_i)$ in the observation point $\boldsymbol{x}_i$ to its neighboring point $\boldsymbol{x'}_i$. A 4-neighborhood system is used.

The likelihood of the true skin surface at position $\boldsymbol{x}_i = (x_i, y_i)$ going through the volumetric point (X_i, Y_i, Z_i), with $Z_i = f(\boldsymbol{x}_i)$ is given as

$$p(V|f_i) \propto V_{\mathrm{y}}(X_i, Y_i, f(\boldsymbol{x}_i)) + c \ , \tag{2}$$

with a shifting constant c, forcing strict positive probabilities. Determining the optimal solution of the given MRF problem is transferred to finding the global maximum of $P(f \mid V)$. The given MRF model consists of $K{\cdot}W$ edges and $K{\cdot}W{\cdot}H$ observation points, thus searching for the global maximum of the joint probability turns out to be a complex task. In order to solve this task in a reasonable amount of time and memory usage, we decided to use an iterative local optimization algorithm. The Iterated Conditional Modes (ICM) approach with the *coding method* of Besag [2] is used because of its ability for fast convergence. The ICM algorithm searches for a local maximum of the joint probability $P(f \mid V)$ by iteratively maximizing each local probability $P(f_i \mid V)$ independently:

$$f_i^{n+1} = \arg\min_z [-\log p(V \mid f_i^n = z) + \textstyle\sum_{\{i,i'\}\in E} (z - f_{i'}^n)^2 / 2\sigma_s^2] \ , \tag{3}$$

where f^0 is an initial guess of the surface. ICM is a local minimization method and the estimation result highly depends on the initial surface guess f^0. Therefore, the initial guess f^0 is retrieved by independently estimating an optimal path for each B-scan using a Markov model, i.e., the same model as for the MRF, but with a 2- instead of a 4-neighborhood system. Finally, the Viterbi algorithm is used for global optimization [12]. Additionally, an annealing procedure inspired by annealing labeling ICM of [10] is used, i.e. allowing the membrane for $n = 0$ to be more relaxed by setting σ_s^0 to a higher value σ_{start} and decreasing it for each L's iteration by $\sigma_s^{n+L} = \max\{\sigma_{\mathrm{end}},\ \sigma_s^n \cdot \sigma_{\mathrm{decr}}\}$.

2.3 Baseline Modeling and Detection with a Hough Transformation

To achieve an appropriate segmentation of the implant base in presence of scanning artifacts, noise, and local vanishing edge structures, a robust and model based segmentation approach was developed using a generalized Hough transform [1]. The applied refractive image undistortion model uses the fact that the axial position of reflections captured with the OCT system matches to the optical path length z_{opt} of light passing through the observed tissue, rather than the geometric path length z_{geo}. Inspired by [11], the relation between z_{opt} and z_{geo} can be approximately formulated as $z_{\mathrm{opt}} = n z_{\mathrm{geo}}$, as shown in Fig. 1(c)–(d), assuming a homogeneous layer with refractive index n. The model used for conversion of optical path length to geometric path length of each axial scan (A-scan, see Fig. 2(a)) is $z = g_u + (g_l - g_u)/n$, where g_u is the known upper position (the skin surface, estimated in Section 2.2), g_l the lower position (base layer), and z denotes the geometric position of the base layer (see Fig. 1(c)).

Given g_u and the constraint of maximal edge intensity support of I_y over g_l, the maximization term for the generalized Hough transform is stated as follows:

$$\max_{Z,n,\theta_X,\theta_Y} \sum_{x,k} I_{\mathrm{y},k}\left(x, g_u(x,k) - [g_u(x,k) - Z_{\theta_X,\theta_Y}(x,k)] \cdot n\right) \quad . \tag{4}$$

The implant base is modeled as a plane with geometric position Z. Since the pin is not located perfectly horizontal, a rotation of the plane in X- and Y-direction is applied to Z, denoted by Z_{θ_X,θ_Y}. As the parameter space is of dimension 4, small discretization step sizes lead to high computation time, i.e. doubling the precision increases the computation time by a factor of 2^4. Since the minimization problem has only one global optimum, which can be distinguished very well from small local extrema, a resolution pyramid approach [7] is applied.

3 Experiments

In this section, a ground truth experiment for verification of the proposed undistortion model, as well as a comparison of the used spoke pattern and dense 3D scanning scheme is performed. We further show results of a quantitative study on several mouse datasets[1]. The B-scans have a dimension of 800 px × 600 px with a lateral distance of the A-Scans of 7.5 µm/px and an axial scale of 4.7 µm/px. Following parameters work best for our datasets: An 11 × 11 median filter, $\sigma_\mathrm{start} = 70$, $\sigma_\mathrm{end} = 10$, $\sigma_\mathrm{dec} = 0.9$, and $L = 5$.

Model Verification: A plane plastic slide is prepared with two glue drops of slightly different size (Vitralit® 4731) with known refractive index of $n = 1.474$. An example image and its segmentation results are shown in Fig. 4. The estimated refractive index of the two glue drops are $n_\mathrm{est} = 1.494$ and $n_\mathrm{est} = 1.507$ respectively. It is assumed that the ground carrier plate is not perfectly planar as expected by the estimation model, causing the deviation from groundtruth.

Scanning Scheme: The spoke pattern scanning scheme is compared with the dense 3D scanning scheme using real mouse recordings. To this end, we use the skin surface reconstructions of scans captured using the spoke pattern with 72 B-scans and the dense 3D scanning scheme, respectively. Figure 5(a) shows reconstructions for a typical skin surface (acquired post mortem). The segmented surface using the spoke pattern is projected onto the dense 3D grid. Small surface differences show the ability of capturing important surface features using the spoke pattern (see Fig. 5(b)). The root mean square deviation (RMSD) is calculated as 1.546 pel. Furthermore, several other surfaces were reconstructed (see Fig. 5(c)). The results show, that using the spoke pattern still leads to good results and preserves many skin details. Moreover, scanning is faster and approximately 91 % of computation time and disk space is saved due to the decreased

[1] All animal experimental procedures have been approved by the local governmental animal care committee (Approval No. 33-42502-04-08/1498).

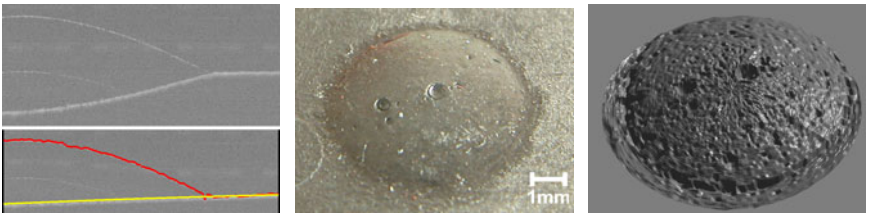

(a) (b) (c)

Fig. 4. Glue drop (Vitralit® 4731) with $n = 1.474$, (a) comparison of original (top) with segmented and undistorted (bottom) OCT B-scan (images cropped), (b) closeup photo of a glue drop, (c) corresponding rendered surface reconstruction

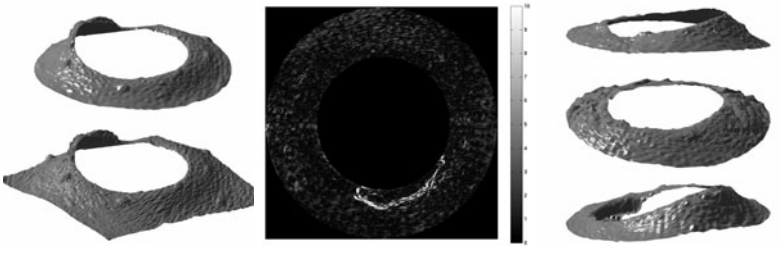

(a) (b) (c)

Fig. 5. (a) Comparison of spoke pattern scanning scheme (top) and dense 3D scanning scheme (bottom), (b) comparison heightmap of absolute surface differences in pel, (c) example skin segmentation results of mouse datasets using spoke pattern

number of B-scans. With 937.5 KiB per image, 666.5 MiB are saved. Skin surfaces of spoke pattern scans are reconstructed using an unoptimized MATLAB implementation in 5.78 min, compared to 68.14 min using dense 3D scans.

Quantitative Study: We further carried out a quantitative analysis on a set of 60 OCT mouse scans of 23 mice at various points of time (including post mortem scans) using the spoke pattern scanning scheme. Manual segmentations of the skin and base were done from experts for 8 OCT images (each 9th slice) per scan, having 3 individual manual segmentations per slice. The experts were instructed to trace only visible parts of the contours. As a metric, we use the RMSD of a surface S_1 towards the mean of a set of surfaces $S_2, \ldots, S_m$. For each B-scan, the RMSD of the automatic skin segmentation towards the mean of all manual skin segmentations is calculated. The average and standard deviation (in pel) over all B-scans is 3.98 ± 3.29. For comparison, the RMSD of each manual skin segmentation towards the mean of all other manual skin segmentations is found as 3.62 ± 1.03. For automatic vs. manual base segmentations, we get: 12.90 ± 18.27 and 3.55 ± 4.51. After outlier removal (B-scans with RMSD >= 10 pel), the RMSD of our fully automated approach is 3.63 ± 1.33 (2.3 % outlier)

and 5.27 ± 2.40 (39.0 % outlier), which is close to the RMSD of the manual segmentation performed by experts with 3.62 ± 1.00 (0.1 % outlier) and 3.21 ± 1.37 (1.4 % outlier). Outliers are mostly due to motion artifacts in scans captured in vivo. Future work will concentrate on reducing the outliers.

4 Conclusion

In this paper we propose a fully automatic approach for 3D segmentation of percutaneous implants using Markov random fields with application to refractive image undistortion. The refraction correction is done by using the subcutaneous implant baseline as a prior for model based estimation of the refractive index using a generalized Hough transform. Several experiments on the undistortion model including a quantitative evaluation show the competitiveness of our algorithm compared to manual segmentation by experts.

References

1. Ballard, D.H.: Generalizing the hough transform to detect arbitraty shapes. Pattern Recognition 13(2), 111–122 (1981)
2. Besag, J.: Spatial interaction and the statistical analysis of lattice systems. Journal of the Royal Statistical Society, B 36, 192–236 (1974)
3. Eichel, J.A., Bizheva, K.K., Clausi, D.A., Fieguth, P.W.: Automated 3D Reconstruction and Segmentation from Optical Coherence Tomography. In: Daniilidis, K., Maragos, P., Paragios, N. (eds.) ECCV 2010, Part III. LNCS, vol. 6313, pp. 44–57. Springer, Heidelberg (2010)
4. Fernández, D.C., Salinas, H.M., Puliafito, C.A.: Automated detection of retinal layer structures on optical coherence tomography images. Optics Express 13(25), 10200–10216 (2005)
5. Garvin, M.K., Abrámoff, M.D., Kardon, R., Russell, S.R., Wu, X., Sonka, M.: Intraretinal Layer Segmentation of Macular Optical Coherenec Tomography Images Using Optimal 3-D Graph Search. IEEE Transactions on Medical Imaging 27(10), 1495–1505 (2008)
6. Hori, Y., Yasuno, Y.: Automatic Characterization and Segmentation of Human Skin using Three-Dimensional Optical Coherence Tomography. Optics Express 14(5), 1862–1877 (2006)
7. Illingworth, J., Kittler, J.: A Survey of the Hough Transform. Computer Vision, Graphics, and Image Processing 44, 87–116 (1988)
8. Karimaghaloo, Z., Shah, M., Francis, S.J., Arnold, D.L., Collins, D.L., Arbel, T.: Detection of Gad-Enhancing Lesions in Multiple Sclerosis Using Conditional Random Fields. In: Jiang, T., Navab, N., Pluim, J.P.W., Viergever, M.A. (eds.) MICCAI 2010. LNCS, vol. 6363, pp. 41–48. Springer, Heidelberg (2010)
9. Kass, M., Witkin, A., Terzopoulos, D.: Snakes: Active Contour Models. International Journal of Computer Vision 1(4), 321–331 (1988)
10. Li, S.Z.: Markov Random Field Modeling in Image Analysis, 3 edn. Springer Publishing Company, Incorporated (2009)
11. Tearney, G.J., Brezinski, M.E., Southern, J.F., Bouma, B.E., Hee, M.R., Fujimoto, J.G.: Determination of the refractive index of highly scattering human tissue by optical coherence tomography. Optics Letters 20(21), 2258–2260 (1995)

12. Viterbi, A.J.: Error Bounds for Convolutional Codes and an Asymptotically Optimum Decoding Algorithm. IEEE Trans. on Inform. Theory 13(2), 260–269 (1967)
13. Westphal, V., Rollins, A.M., Radhakrishnan, S.: Correction of geometric and refractive image distortions in optical coherence tomography applying Fermats principle. Optics Express 10(9), 397–404 (2002)
14. Yazdanpanah, A., Hamarneh, G., Smith, B., Sarunic, M.: Intra-retinal Layer Segmentation in Optical Coherence Tomography Using an Active Contour Approach. In: Yang, G.-Z., Hawkes, D., Rueckert, D., Noble, A., Taylor, C. (eds.) MICCAI 2009, Part II. LNCS, vol. 5762, pp. 649–656. Springer, Heidelberg (2009)